Quantum transport of the internal state of Kr^{35+} ions through amorphous carbon foils

Tatsuya Minami
Department of Physics and Astronomy, University of Tennessee, Knoxville, Tennessee 37996-1200

Carlos O. Reinhold
Physics Division, Oak Ridge National Laboratory, Oak Ridge, Tennessee 37831-6373

Marek Seliger and Joachim Burgdörfer
Institute for Theoretical Physics, Vienna University of Technology, A-1040 Vienna, Austria
and Department of Physics and Astronomy, University of Tennessee, Knoxville, Tennesse 37996-1200

Claude Fourment, Emily Lamour, Jean-Pierre Rozet, and Dominique Vernhet
GPS, CNRS UMR 77-88, Universités Paris 7 et 6, 75251 Paris, Cedex 05, France

Benoit Gervais
CIRIL, CEA-CNRS-ISMRA, UMR 66-37 rue Claude Bloch, BP 5133 14070 Caen, Cedex 05, France
(Received 14 September 2001; published 5 February 2002)

The population dynamics of the internal state of 60 MeV/u Kr^{35+} ions traversing amorphous carbon foils is studied theoretically and experimentally. This system is of particular interest as the times scales for collisional distribution, mixing due to the wake field, and radiative processes are comparable to each other. A transport theory based on a quantum-trajectory Monte Carlo method is developed, which treats the collisional and radiative redistribution of states on the same footing. The simulations exhibit clear signatures for the interplay between radiative decay and collisional mixing. Good agreement with experimental data is found.

DOI: 10.1103/PhysRevA.65.032901 PACS number(s): 34.50.Fa, 34.10.+x

I. INTRODUCTION

The internal state of a fast atom/ion traversing solids is an example of an open quantum system. The large number of degrees of freedom of the environment refers here to the solid and, as discussed below, also to the radiation field. The open quantum system is a hydrogenic one-electron ion with three degrees of freedom (without spin). For such a system accurate comparisons between theory and experiment are possible and, therefore, pursuing this problem augments our conceptual understanding of the dynamics of open quantum systems.

When the ion travels through the solid, the electron bound to the ion interacts with the solid through a variety of processes. One is a nondissipative interaction originating from the induced screening potential, which is due to the response of the electrons in the solid to the large positive charge of the ion. The effective electric field produced by this screening charge is referred to as the wake field [1,2]. It induces a Stark-like mixing among the atomic orbitals of the ion (mostly within a given energy shell) [3,4] and can be described by the complex dielectric function ϵ. The imaginary part of $-1/\epsilon$, on the other hand, represents dissipative interactions due to collisions between the electron in the ion and particles in the solid, i.e., electrons and screened nuclei in the solid [5]. These collisions transfer energy to particles in the solid and, also, mix and excite the atomic orbitals of the impinging ion [6–12]. Recently [13,14], we have developed a quantum-mechanical transport theory (QTT) for the collision-induced dynamics of the internal state and applied it to H and Ar^{17+} traversing amorphous carbon foils. The QTT makes use of the fact that if the ion velocity is very high, each individual collision can be described using perturbation theory. The roles of the different collisional interactions have been studied in detail in [13,14,25].

In this paper, we focus on the case of Kr^{35+} $(1s)$ traversing amorphous carbon foils with a kinetic energy of 60 MeV/u. Experimental studies for this system have recently been performed and briefly reported in Ref. [15]. This collision system is of particular interest for several reasons. First, previous work considered fully stripped ions. This leads to uncertainties in the initial state of the one-electron ion created inside the solid as a result of an initial electron-capture event whose accurate theoretical treatment remains a challenge. For the present system, the initial internal state of the ion is a deeply bound and nondegenerate ground state and, thus, well defined. Secondly, the fine-structure splittings and the Lamb shifts of the internal states of Kr^{35+} are sufficiently large due to the high charge of the nucleus that cannot be neglected during transport. For example, the fine-structure splitting between $3p_{1/2}$ and $3p_{3/2}$ is 0.867 a.u. and the Lamb splitting between $3s_{1/2}$ and $3p_{1/2}$ is 0.0190 a.u. while the coupling strength between $3s$ and $3p$ due to the wake field is about 0.0118 a.u. [16]. Therefore, the fine-structure splittings strongly suppress the Stark mixing by the wake field between the atomic states with different total angular momentum j (e.g., between $s_{1/2}$ and $p_{3/2}$). Additionally, the Lamb shift modifies the extent of mixing even between the states with same j (i.e., between $s_{1/2}$ and $p_{1/2}$ and so on). This

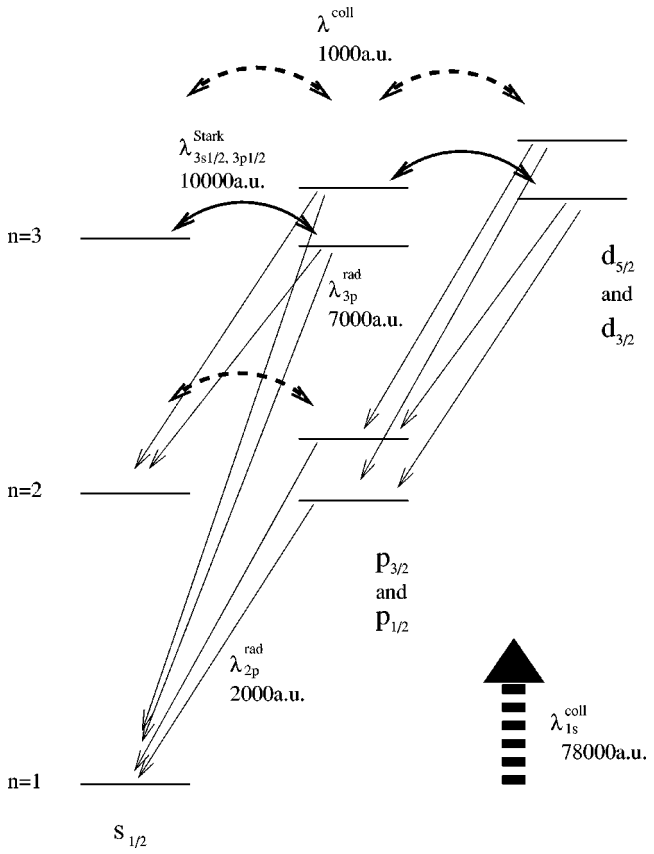

FIG. 1. Schematic diagram for the characteristic distances of the different events which can alter the populations of the internal state of a Kr^{35+} ion with a velocity $v_p=47$ a.u.. The mean free paths depicted correspond to Stark mixing time t_s (path $d=v_p t_s$) between the $3p_{1/2}$ and the $3s_{1/2}$ states, $\lambda^{\mathrm{Stark}}_{3s_{1/2},3p_{1/2}}$, the radiative decay length of the $2p$ and $3p$ states, $\lambda^{\mathrm{decay}}_{2p}$ and $\lambda^{\mathrm{decay}}_{3p}$, the collisional mean free path for free electrons, λ^{coll}, and the collisional decay length (or excitation path) of the $1s$ state to all states, $\lambda^{\mathrm{coll}}_{1s}$.

delicate balance between the fine-structure splittings, the Lamb splittings, and the wake field is one of the distinctive features of Kr^{35+} ions as compared, for example, to Ar^{17+} or H.

The most important distinctive feature of the present collision system involving Kr^{35+} ions is, however, the short lifetime of the excited internal states against spontaneous radiative decay, which becomes comparable to the dwell time inside the foil for typical foil thicknesses used in the experiment. Unlike collisions, which predominantly excite the electron to higher energy levels, radiative decay deexcites the electron and thereby modifies the dynamics of the internal state of the ion during its passage through the foil. As will be shown below, this leads to dramatic changes in the populations of excited states of the ion at the foil exit. In fact, Stark mixing, collisional mixing, and radiative decay occur all on comparable time scales. The schematic diagram in Fig. 1 illustrates these time scales expressed in terms of propagation mean free paths for each process, i.e., $\lambda=\Delta t v_p$, where Δt is the characteristic time of these processes and $v_p=47$ a.u. is the velocity of the ion. In this paper we present an extension of our previously developed QTT [13,14], which incorporates collisional and radiative redistribution processes on equal footing and a comparison with experimental results for Kr^{35+}. To probe the dynamics of the internal state of the ion experimentally, we measure the total intensity of x rays emitted from the ion. Varying the foil thickness, we can obtain partial information on the time evolution of the populations of excited states created by the ion-solid interaction. Experimental intensities of x rays are compared with the prediction of our QTT.

This paper is organized as follows. In Sec. II we briefly present the main ingredients of our QTT. A more detailed account will be given elsewhere [17]. In Sec. III, a brief description of the experiment is given. In Sec. IV, we compare the calculated intensities with experiment for Kr^{35+} passing through carbon foils and compare the calculated intensities with experiment. The last section is devoted to an outlook. Atomic units are used throughout unless otherwise stated.

II. THEORY

We shall consider the transmission of a fast hydrogenlike ion with nuclear charge Z_p and velocity v_p through an amorphous foil with a given thickness d. Even though the framework of our treatment is general, we will focus on the specific example of Kr^{35+} ions ($Z_p=36$) traversing C foils at a velocity $v_p=47$ a.u.. We will study the evolution of a single active electron carried by the ion. We use a frame of reference moving with the ion. We use time t and path length of propagation in the laboratory frame, d, interchangeably, since $d=v_p t$ and v_p can be treated as a constant. The latter takes into account the fact that the slowing down of the ion at this speed, and for the foil thicknesses under consideration, can be safely neglected. The zero point $t=0$ ($d=0$) corresponds to the time at which the ion enters the foil. For simplicity, we will often use a single index $|i\rangle$ to label the eigenstates of the ion in vacuum with the implicit understanding that $|i\rangle=|n\ell jm_j\rangle$, where n is the principal quantum number, ℓ is the orbital angular momentum, and j and m_j are the total angular momentum and its projection onto the z axis. The quantization axis corresponds to the direction of propagation (i.e., z axis $\|\vec{v}_p$).

In order to describe the time evolution of the internal state of the ion, we should consider the time evolution of the entire system including its environment, that is, the hydrogenlike ion, the amorphous carbon foil and the electromagnetic field. If we denote a mixed state of the total system at a certain time t by a density operator $\rho(t)$, the time evolution of the state is governed by the Liouville–von Neumann equation,

$$i\frac{\partial}{\partial t}\rho(t)=[\mathcal{H}_{\mathrm{tot}},\rho(t)], \tag{2.1}$$

where $\mathcal{H}_{\mathrm{tot}}$ is the Hamiltonian of the total system. Such an approach is prohibitively complicated to implement in view of the large number of degrees of freedom. Instead, we invoke an open-quantum-system approach. We consider the subsystem of the internal state of the ion explicitly as the

open system and treat all remaining degrees of freedom as ''environment.'' The open system is described by a reduced density matrix $\sigma(t)$, which results from tracing out from $\rho(t)$ all degrees of freedom except those of the internal states,

$$\sigma(t) \equiv \mathrm{Tr}'[\rho(t)], \tag{2.2}$$

where Tr' denotes the partial trace over all degrees of freedom of the environment. From this reduced density matrix $\sigma(t)$, we can obtain the expectation value of any observable A of the internal system at any arbitrary time t as $\langle A(t)\rangle = \mathrm{Tr}'[A\sigma(t)]$. In particular, the population or occupation probability P of state $|i\rangle$ is given by $(A=|i\rangle\langle i|)$,

$$P_i(t) = \langle i|\sigma(t)|i\rangle. \tag{2.3}$$

The time evolution of $\sigma(t)$ is governed by a Liouville–von Neumann equation with a dissipative term

$$i\frac{\partial}{\partial t}\sigma(t) = [\mathcal{H}_{\mathrm{atom}}, \sigma(t)] + \mathcal{R}\sigma(t), \tag{2.4}$$

where $\mathcal{R}$ is a relaxation superoperator that represents the interaction between the electron and the environment, consisting of the particles in the foil and the electromagnetic field. In the above equation, $\mathcal{H}_{\mathrm{atom}}$ is a time-independent Hermitian Hamiltonian describing the nondissipative evolution of the electron in the ion,

$$\mathcal{H}_{\mathrm{atom}} \equiv \frac{p^2}{2} - \frac{Z_p}{r} + \Delta\mathcal{H}_{\mathrm{rel}} + V_{\mathrm{scr}}(\vec{r}), \tag{2.5}$$

where r and p are the position coordinate and the momentum of the electron in a reference frame fixed to the ion, and $\Delta\mathcal{H}_{\mathrm{rel}}$ represents relativistic and Lamb-shift corrections. In Eq. (2.5), $V_{\mathrm{scr}}(\vec{r})$ denotes the screening potential or wake potential induced by the ion. For convenience, we define $\mathcal{H}_0$ as the internal Hamiltonian of the ion in vacuum.

$$\mathcal{H}_0 \equiv \frac{p^2}{2} - \frac{Z_p}{r} + \Delta\mathcal{H}_{\mathrm{rel}}, \tag{2.6}$$

whose eigenvalues and eigenenergies are given by

$$\mathcal{H}_0|i\rangle = E_i|i\rangle \tag{2.7}$$

with $(i=nljm_j)$,

$$E_i = \mu c^2\left\{\left[1+\left(\frac{Z_p\alpha}{n-j-\frac{1}{2}+[(j+\frac{1}{2})^2-Z_p^2\alpha^2]^{1/2}}\right)^2\right]^{-1/2}-1\right\} + E_i^{\mathrm{Lamb}}. \tag{2.8}$$

μ denotes the reduced mass of the electron, c is the speed of light, α is the fine-structure constant, and E_i^{Lamb} is the Lamb shift [18].

The explicit determination of $\mathcal{R}$ requires drastic approximations. The central simplifying assumption, which makes the determination of $\mathcal{R}$ feasible, is the validity of linear response theory, i.e., the response of the environment can be treated in first-order perturbation theory. As a result of the Born approximation, the dynamics of the bath variables remain decoupled from the internal state σ of the subsystem. The important point to be noted, however, is that no weak-perturbation assumption is implied for the back reaction onto the subsystem. In fact, in the present context we will consider strong coupling that precludes a perturbative treatment of the evolution of the internal degrees of freedom under the influence of $\mathcal{R}$. The second assumption is the Markov approximation, that is, the neglect of memory effects. Only the instantaneous state of the system determines its relaxation while retardation effects can be neglected. Both approximations are consistent with the assumption that the characteristic time scale for the system-environment interaction, the relaxation time, is long compared to the intrinsic time scale of the reversible dynamics in the environment.

Even after the evaluation of $\mathcal{R}$ within linear response theory, solving the Liouville equation is a tedious task. One standard method consists of solving the Liouville equation by means of an expansion of the density matrix in a truncated basis set of states $|\chi_i\rangle$, $i=1,2,...,N$, where N is the rank of the expansion in the Hilbert state. This reduces the Liouville equation to a finite system of N^2 coupled equations for N^2 matrix elements entailing an N^4 numerical effort. Even though in the present case the coupling to the continuum (that is, ionization) is quite small and the truncated basis subtends only the bound-state portion of the internal-state space, N becomes quite large. This makes the explicit solution of the Liouville–von Neumann equation difficult. In order to circumvent this problem, Rozet *et al.* [16] made a selection of a small number of nonvanishing off-diagonal elements of σ such that the dominant elements of $\mathcal{R}$ could be easily stored in memory. In this paper, we adopt an alternative method, which keeps all elements of σ and all couplings to the environment but avoids dealing directly with a finite representation of $\mathcal{R}$. This method consists of describing the dynamics of the open quantum systems in terms of a stochastic Schrödinger equation, which can be solved by a quantum-trajectory Monte Carlo (QTMC) method. In the limit of a large number of Monte Carlo realizations this method becomes equivalent to solving Eq. (2.4) directly, but involves only matrices with dimension N^2. This method is the quantum analog of the corresponding classical transport theory [5]. It is also closely related to the so-called Monte Carlo wave-function (MCWF) method in quantum optics [19,20]. In fact, in our treatment of the radiative process we will explicitly exploit this similarity. A detailed account of the similarities and differences between stochastic Schrödinger equations for radiative and collisional processes will be given elsewhere [17]. The full treatment of the transport problem for the internal states in terms of a QTMC solution of a stochastic Schrödinger equation containing both collisional and radiative processes will be referred to as QTT.

The reduced density matrix $\sigma(t)$ can be decomposed into an incoherent average over time-evolved pure states starting from certain initial conditions [21]. If the electron is initially, at $t=0$, in a pure state,

$$\sigma(t)=\frac{1}{N_{\rm traj}}\sum_{\mu=1}^{N_{\rm traj}}\sigma^{\mu}(t), \tag{2.9}$$

where $N_{\rm traj}$ denotes the number of quantum trajectories of pure states involved in the average. In Eq. (2.9), each $\sigma^{\mu}(t)$ denotes a pure state that can be rewritten in terms of its corresponding wave function as

$$\sigma^{\mu}(t)=|\psi^{\mu}(t)\rangle\langle\psi^{\mu}(t)|. \tag{2.10}$$

Since the ion is initially in a pure state $|i_0\rangle$, the initial condition for the wave function is

$$|\psi^{\mu}(t=0)\rangle=|i_0\rangle. \tag{2.11}$$

The index μ labels the quantum trajectory. Different quantum trajectories describe different random sequences of interactions with the environment. In the present collision system, we assume either $|i_0\rangle=|1s\frac{1}{2}\frac{1}{2}\rangle$ or $|i_0\rangle=|1s\frac{1}{2}-\frac{1}{2}\rangle$ since the results are independent of the initial spin of the electron. For more general problems in which the electron is initially not in a pure state, the average (Eq. 2.9) would, in addition, involve a weighted average over different initial conditions determined by the initial density matrix $\sigma(t\rightarrow 0)$ (see, e.g., [13]). In numerical simulations, the total number of quantum trajectories, $N_{\rm traj}$, has to be sufficiently large such that the right-hand side of Eq. (2.9) converges. The stochastic time evolution of the quantum trajectories is calculated by constructing their corresponding time-evolution operator $U^{\mu}(t,0)$ such that

$$|\psi^{\mu}(t)\rangle=U^{\mu}(t,0)|i_0\rangle. \tag{2.12}$$

We decompose the time-evolution operator into a sequence of products of two types of evolution operators,

$$U^{\mu}(t,0)=U^{\mu}_{\rm cont}(t,t_n)\prod_{k=1}^{n}U^{\mu}_{\rm dis}(t_k)U^{\mu}_{\rm cont}(t_k,t_{k-1})\quad(t_0=0). \tag{2.13}$$

One factor, $U^{\mu}_{\rm cont}(t_{k+1},t_k)$, stands for a continuous change of the wave function during the time period $[t_{k+1},t_k]$ in between stochastic processes. The other factor, $U^{\mu}_{\rm dis}(t_k)$, represents a discontinuous change of the wave function, a quantum jump, at randomly chosen times $t=t_k$. Finite-dimensional representations of these operators have dimension N^2 and are easier to treat numerically than the full representation of $\mathcal{R}$ in Eq. (2.4).

In the following two sections, we briefly sketch the construction of U^{μ} in Eq. (2.13) for radiative decay and collisions. The set of random times $\{t_k\}$ is therefore subdivided into independent subsets $\{t_k^{\rm rad}\}$ and $\{t_k^{\rm coll}\}$, one for each process.

A. Radiative decay

For radiative decay during transport within our QTT approach we employ a variant of the so-called MCWF method [19,20], recently developed in quantum optics. The MCWF method was first introduced by Dalibard, Castin, and Mølmer [19] in a time-differential form. Subsequently, Dum, Zoller, and Ritsch introduced an equivalent method in a time-integrated form [20]. Since our transport formalism is based on finite time-evolution steps [Eq. (2.13)], it is most convenient to adopt the formalism of [20] for the present problem.

The evolution operator within the MCWF method can be decomposed precisely as in Eq. (2.13). The discontinuous jump operator, $U^{\mu}_{\rm dis}$, corresponds to a sudden projection of the wave function onto a final state, ''the collapse of the wave function,'' after a radiative decay event. At $t=t_k^{\rm rad}$ a photon is emitted corresponding to a transition onto a state $|j\rangle$,

$$|\psi^{\mu}(t_k^{\rm rad}+\delta t)\rangle=U^{\mu}_{\rm dis}(t_k^{\rm rad})|\psi^{\mu}(t_k^{\rm rad}-\delta t)\rangle, \tag{2.14}$$

$$=|j\rangle, \tag{2.15}$$

where $\delta t\rightarrow 0$ is an infinitesimal time step. Thus, the problem is reduced to determining the decay times $t_k^{\rm rad}$, the decay probabilities, and the states into which the system collapses at these times.

The continuous evolution described by $U^{\mu}_{\rm cont}$ by a non-Hermitian Hamiltonian [22] is followed by normalization of the wave function. The time evolution of the wave function during a time period Δt is given by

$$|\psi^{\mu}(t+\Delta t)\rangle=U^{\mu}_{\rm cont}(t+\Delta t,t)|\psi^{\mu}(t)\rangle=\frac{\exp(-i\mathcal{H}_{\rm eff}\Delta t)|\psi^{\mu}(t)\rangle}{\langle\psi^{\mu}(t)|\exp(-\mathbf{\Gamma}\Delta t)|\psi^{\mu}(t)\rangle}, \tag{2.16}$$

where $|\psi^{\mu}(t)\rangle$ is the wave function of the system at time t. The effective Hamiltonian governing the continuous evolution between quantum jumps is given by

$$\mathcal{H}_{\rm eff}\equiv\mathcal{H}_{\rm atom}-\frac{i}{2}\mathbf{\Gamma}, \tag{2.17}$$

where the operator $\mathbf{\Gamma}$ describes the decay of each atomic state in first order in the coupling to the radiation field. In the basis of states $|i\rangle(\equiv|n,\ell,j,m_j\rangle)$ that diagonalizes $\mathcal{H}_0$ [Eq. (2.7)], $\mathbf{\Gamma}$ is diagonal to first order in the coupling to the radiation field [22]

$$\langle i|\mathbf{\Gamma}|j\rangle=\Gamma_i\delta_{ij}, \tag{2.18}$$

where $\delta_{i,j}$ is a Kronecker delta and Γ_i is the decay rate of the state $|i\rangle$, which is given by the sum of all partial transition rates $\Gamma_{i\rightarrow k}$ from state $|i\rangle$ to all allowed states $|k\rangle$

$$\Gamma_i=\sum_k\Gamma_{i\rightarrow k}. \tag{2.19}$$

In the electric-dipole approximation [23]

$$\Gamma_{i\rightarrow k}=\frac{4(E_i-E_k)^3}{3c^2}|\langle i|\vec{r}|k\rangle|^2\Theta(E_i-E_k), \tag{2.20}$$

where Θ is a unit step function such that $\Gamma_{i\to k}=0$ if $E_i < E_k$. For highly charged ions, relativistic corrections beyond the electric-dipole approximation are not negligible. We incorporate these corrections for Lyman and Balmer decay following the work of Pal'chikov [24].

The present method for determining $U_{\rm dis}$ differs from Ref. [20] in that we employ Poissonian sampling of decay times $\{t_k^{\rm rad}\}$ corresponding to an exponential lifetime distribution rather than a sampling of the actual lifetime distribution for each state, which requires the explicit calculation of the ''delay-time'' function of all (perturbed) states. This method is computationally advantageous, in particular, for multidecay-channel-state systems as opposed to few-state systems usually encountered in quantum optics. To this end, we subdivide the set of decay times into subsets $\{t_k^{\rm rad}\} \equiv \{\{t_k^{i\to j}\}; i,j=1,2,...,N\}$. Each subset $\{t_k^{i\to j}\}$ represents the random sequence of times at which a photon could be emitted for a specific decay channel $i\to j$. Therefore, the decay times are obtained by sampling multiple random time intervals $\Delta t_k^{i\to j}$ for each decay channel $i\to j$ according to Poisson distributions

$$\mathcal{P}(\Delta t_k^{i\to j})=\Gamma_{i\to j}\exp(-\Gamma_{i\to j}\Delta t_k^{i\to j}). \tag{2.21}$$

Accordingly, the time for the next quantum jump $i\to j$ (or collapse of the wave function) is given by

$$t_k^{i\to j}=t_{k-1}^{i\to j}+\Delta t_k^{i\to j}. \tag{2.22}$$

The process takes place subject to the condition imposed by the occupation probability of the state $|i\rangle$,

$$P_i(t_k^{i\to j})\equiv|\langle i|\psi^\mu(t_k^{i\to j}-\delta t)\rangle|^2. \tag{2.23}$$

Therefore, another random number ϵ is chosen that is uniformly distributed in the interval (0,1) such that

$$|\psi^\mu(t_k^{i\to j}+\delta t)\rangle=U_{\rm dis}^\mu(t_k^{i\to j})|\psi^\mu(t_k^{i\to j}-\delta t)\rangle \tag{2.24}$$

$$=\begin{cases}|j\rangle & \text{if } \epsilon<P_i(t_k^{i\to j})\\ |\psi^\mu(t_k^{i\to j}-\delta t)\rangle & \text{if } \epsilon>P_i(t_k^{i\to j})\end{cases}. \tag{2.25}$$

We refer to the steps [Eq. (2.15), (2.16), and (2.25)] as the QTMC method for the radiative stochastic process.

B. Multiple collisions

The interactions between the projectile electron and the solid-state environment provide a strong competing channel for the redistribution of the occupation amplitude among internal states. We treat these processes on equal footing with the radiative processes. They can be described also in terms of a stochastic Schrödinger equation whose solution can be generated in a corresponding QTMC method in close analogy to the radiative process.

When the electron in the ion collides with screened nuclei in the solid, the energy transferred to the nucleus can be neglected due to its large mass. We refer to this subset of collisions as elastic collisions. On the other hand, when the electron in the ion collides with electrons in the solid, the energy transferred to the target electron is not negligible. Thus we refer to these collisions as inelastic collisions. It should be noted that this terminology refers to the target frame. In the frame of the projectile both elastic and inelastic collisions lead to energy transfer to the projectile electron. Due to these collisions, the electron, initially in the $1s$ orbital, is excited to higher-lying states. Successive collisions induce intrashell and intershell mixing and drive the system toward the statistical mixing limit. The treatment of multiple collisions within the QTT by means of a QTMC technique has been described in Refs. [13,14]. We therefore only briefly summarize the main ingredients and necessary extensions for highly charged ions.

Much like the procedure described for radiative decay, one determines the random time intervals between quantum jumps and the quantum-jump operators associated with collisions. The random jump times are directly related, within linear response theory, to the collisional transition rates [2]

$$\Gamma_{i\to k}^{\rm coll}=v_p\int d\omega\, d\vec{q}\,|\langle k|\exp(i\vec{q}\cdot\vec{r})|i\rangle|^2\frac{d^4\lambda^{-1}}{d\omega\, d\vec{q}} \times\delta(E_k-E_i+\omega-\vec{v}_p\cdot\vec{q}), \tag{2.26}$$

$$\Gamma_i^{\rm coll}=\sum_i\Gamma_{i\to k}^{\rm coll}, \tag{2.27}$$

where $d^4\lambda^{-1}/d\omega\, d\vec{q}$ represents either the elastic or the inelastic differential inverse mean free path for transport of free electrons as a function of the energy transferred to the solid, ω, ($\omega=0$ for elastic collisions) and the momentum gained by the solid, $\vec{q}$. Details concerning the calculation of $d^4\lambda^{-1}/d\omega\, d\vec{q}$ for carbon foils can be found in Refs. [25,26].

There exist a few differences between radiative and collisional mixing. First, in contrast to the dipole operator, which governs radiative decay [Eq. (2.20)], the form factor governing collisions in Born approximation [Eq. (2.26)] does not obey selection rules that severely limit the number of active reaction channels. While radiative decay as an explicitly exothermic reaction channel leads to a reduction of the degree of excitation corresponding to a reduction of the populated Hilbert subspace, collisional transitions can be both exothermic and endothermic resulting in an increased spread of the wave packet over larger and larger subspaces of the internal-state space (including the continuum). This fact leads not to only additional complications (N becomes very large) but also to simplifications.

The central simplifying assumption utilized in previous works [13,14], which makes the collisional problem tractable, is the quasifree-electron approximation. The basic idea is that if the projectile is fast enough and collisional interaction times are sufficiently short the electron can be considered to be free during the interaction. This is equivalent to the assumption of the impulse approximation. Consequently, the strength of the collisional interaction is not necessarily required to be small. The random sequence of decay times $\{t_k^{\rm coll}\}$ at which $U_{\rm dis}^\mu$ is applied is obtained from a single Poisson distribution for time intervals $\Delta t_k^{\rm coll}\equiv t_k^{\rm coll}-t_{k-1}^{\rm coll}$,

$$\mathcal{P}(\Delta t_k^{\rm coll}) = \Gamma^{\rm coll} \exp(-\Delta t_k^{\rm coll} \Gamma^{\rm coll}), \tag{2.28}$$

$$\Gamma^{\rm coll} = v_p / \lambda^{\rm coll}, \tag{2.29}$$

$$\frac{1}{\lambda^{\rm coll}} = \int d\omega\, d\vec{q} \frac{d\lambda^{-1}}{d\omega\, d\vec{q}} \delta(\omega - \vec{v}_p \cdot \vec{q}). \tag{2.30}$$

where $\lambda^{\rm coll}$ is the total elastic or inelastic collisional mean free path for free electrons, integrated over all $\vec{q}$ and ω.

The important consequence of the quasifree-electron approximation [Eqs. (2.28)–(2.30)] is that the collisional mean free path is independent of the internal state occupied at the transition time $t = t_k^{\rm coll}$. The quantum jump is described by $U_{\rm dis}^{\mu}(t_k^{\rm coll})$ corresponding to an impulsive momentum transfer $\vec{q}_k$ delivered to the electron, i.e.,

$$|\psi^{\mu}(t_k^{\rm coll} + \delta t)\rangle = U_{\rm dis}^{\mu}(t_k^{\rm coll}) |\psi^{\mu}(t_k^{\rm coll} - \delta t)\rangle. \tag{2.31}$$

$$= \exp(i \vec{q}_k \cdot \vec{r}) |\psi^{\mu}(t_k^{\rm coll} - \delta t)\rangle, \tag{2.32}$$

where $\vec{q}_k$ is chosen at random from the probability density

$$\mathcal{P}(\vec{q}) \propto \frac{d\lambda^{-1}}{d\vec{q}}. \tag{2.33}$$

Finally, since a single mean free path is assumed, the continuous-time-evolution operator in Eq. (2.16) is unitary without renormalization. Note that in the (unphysical) limit, the radiative decay rates for all states would be identical, the continuous-evolution operator $U_{\rm cont}^{\mu} = \exp(-i\mathcal{H}_{\rm atom}\Delta t)$ [Eq. (2.16)] would also become explicitly unitary.

The quasifree electron approximation can be modified for deeply bound states of highly charged ions without changing the algorithm for the stochastic sequence of collision times [Eq. (2.30)] by incorporating the constraint $q \geqslant \text{const} = |q_{\|}|$ on momentum transfers resulting from the δ function in Eq. (2.26), which yields

$$q_{\|} = (E_j - E_i + \omega)/v_p. \tag{2.34}$$

We choose the absolute magnitude of the momentum transfer $\vec{q}$ at random according to the probability density (2.33) and we apply an n-dependent momentum boost to the electron whose matrix elements in the $\{n,l,j,m_j\}$ representation are given by

$$\langle n,l,j,m_j | U_{\rm dis}^{\mu} | n',l',j',m_j' \rangle \equiv \langle n,l,j,m_j | \exp(\vec{q}_{n,n'} \cdot \vec{r}) | n',l',j',m_j' \rangle, \tag{2.35}$$

with

$$\vec{q}_{n,n'} \equiv \begin{cases} (q_{\perp} \cos\phi, q_{\perp} \sin\phi, q_{\|}) & \text{if } q_{\|} \leqslant q \\ 0 & \text{if } q_{\|} > q, \end{cases} \tag{2.36}$$

$$q_{\perp} \equiv \sqrt{\Delta\vec{q}^2 - q_{\|}^2}. \tag{2.37}$$

In the above equations, ϕ is a random angle chosen uniformly in the interval $(0,2\pi)$. We neglect relativistic corrections to $E_{i,j}, q_{\|}$ and hence $\vec{q}$ is only dependent on n,n'.

C. Calculation of photon intensities

The total photon intensity, (i.e., the number of photons) associated with a particular radiative decay channel, $i \to k$, and the total intensity of all photons emitted from a particular level are given by

$$I_{i\to k} = \Gamma_{i\to k} \int_0^{\infty} dt\, P_i(t) \tag{2.38}$$

and

$$I_i = \Gamma_i \int_0^{\infty} dt\, P_i(t), \tag{2.39}$$

respectively. These intensities provide direct information on the time-integrated populations $P_i(t)$ (weighted by a constant transition rate). Note that the time integral involves the population while the ion is both inside the solid and after foil exit. The population of excited states is initially zero, increases due to excitation inside the foil, and tends to zero again for $t \to \infty$ when the atom relaxes to the ground state by radiative decay after foil transmission. Since transport through foils of different thicknesses yield different intermediate populations, changes in the intensities provide direct evidence of the changing populations due to transport. Since energy levels are independent of m_j, the experimentally observable intensities correspond to

$$I_{n,l,j} = \sum_{m_j} I_{n,\not{l},j,m}, \tag{2.40}$$

which provide direct information on the populations of the n, l, j subshells.

In practice, the time evolution of the populations is explicitly evaluated using the QTT only while the ion is inside the foil. In free space the effect of residual coherences is negligible and the Liouville equation reduces to a system of rate equations for the state populations [i.e., the diagonal matrix elements of the density matrix, Eq. (2.3)],

$$\frac{d}{dt} P_j(t) = \sum_{i \neq j} \Gamma_{i\to j} P_i(t) - \Gamma_j P_j(t) \quad (t \geqslant d/v_p). \tag{2.41}$$

Thus, the time evolution of the populations after foil exit is most easily evaluated by solving the system of rate equations (2.41). The initial conditions of Eqs. (2.41) at $t = d/v_p$ are given by the populations of zero-field eigenstates at foil exit.

III. EXPERIMENT

Our experiment has been performed at GANIL (Grand Accélérateur National d'Ions Lourds) on the LISE (Ligne d'Ions Super Epluchés) facility. The experimental set-up has been already described in detail elsewhere [27]. Here we

TABLE I. Labeling and branching ratios of the Balmer lines.

Transition	Label	Branching ratio
$3s_{1/2}\rightarrow 2p_{3/2}$	Ba_1	0.644 85
$3d_{3/2}\rightarrow 2p_{3/2}$	Ba_2	0.153 79
$3d_{5/2}\rightarrow 2p_{3/2}$	Ba_3	1
$3p_{1/2}\rightarrow 2s_{1/2}$	Ba_{4a}	0.120 87
$3s_{1/2}\rightarrow 2p_{1/2}$	Ba_{4b}	0.355 15
$3p_{3/2}\rightarrow 2s_{1/2}$	Ba_{5a}	0.123 40
$3d_{3/2}\rightarrow 2p_{1/2}$	Ba_{5b}	0.846 21

summarize its main characteristics. Beams are directed onto self-supported amorphous carbon foils with measured thicknesses and purity [27]. The foils can be tilted to fine-tune the effective transport thickness. Foil thicknesses are changed from 3 to 220 $\mu g/cm^2$ to study the ion transport from the near-single-collision limit to the equilibrium limit. Balmer α lines are measured using high-resolution high-transmission Bragg-crystal spectrometers. Each photon detection system is placed at a specific angle with respect to the beam direction to assure polarization insensitivity of the measurements.

From the Balmer lines and branching ratios (see Table I), we can obtain the ratio between the total intensities of photons emitted from the $3p_{1/2}$ and $3s_{1/2}$ states,

$$\frac{I_{3p_{1/2}}}{I_{3s_{1/2}}}=\frac{1}{0.1874}\left(\frac{\mathrm{Ba}_4}{\mathrm{Ba}_1}-0.5507\right) \tag{3.1}$$

and from the $3d_{3/2}$ and $3d_{5/2}$ states,

$$\frac{I_{3d_{3/2}}}{I_{3d_{3/2}}}=6.502\frac{\mathrm{Ba}_2}{\mathrm{Ba}_3}. \tag{3.2}$$

Details of this analysis are given in Ref. [27]. Differences between the coefficients above and those in Ref. [27] are due to the relativistic corrections to the radiative transition rates taken into account in the present work.

IV. RESULTS

In this section we present the application of the quantum transport theory introduced in Sec. II to the case of 60 MeV/u Kr^{35+} $(1s)$ ions interacting with carbon foils. We begin by performing a simplified analysis of the time evolution of the internal state of the ion in the absence of multiple collisions in order to highlight the modifications due to radiative decay, the subshell splittings of the energy levels, and their interplay with the intrashell mixing due to the wake field.

For simplicity, we choose a three-level system with two coupled upper levels (states $|1\rangle$ and $|2\rangle$) and one lower level (state $|3\rangle$) to which radiative decay occurs. The benefit of first investigating this simplified system is that its time evolution can be evaluated analytically. Therefore, it can be used to test the accuracy of the QTMC approach described in the preceding section. In addition, much can be understood concerning the relative importance of the wake field and the subshell splittings in the population dynamics of excited states. If we write the projection of the wave function onto the upper two levels of this model system as

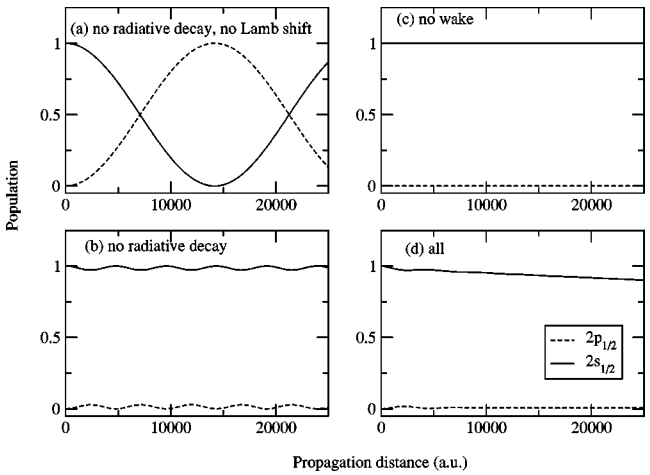

FIG. 2. Population dynamics in the $n=2$ shell obtained within a three-state model involving the $2s_{1/2}$ and $2p_{1/2}$ states as upper levels and the $1s_{1/2}$ state as the lower level. The calculations in (d) include the parameters of the upper levels that control the time evolution in Kr^{35+}: the Lamb shift, $|\Delta E|=6.3\times10^{-2}$, the radiative decay rates $\Gamma_{2s_{1/2}}=0$, $\Gamma_{2p_{1/2}}=2.5677\times10^{-2}$ [16], and the Stark coupling due to the wake field, $w=5.43\times10^{-3}$ [16], all in a.u. Some of these parameters are set to zero in (a), (b), and (c). Initially, at $d=0$, $P_{2s_{1/2}}(0)=1$, $P_{2p_{1/2}}(0)=0$, and $P_{1s_{1/2}}(0)=0$.

$$|\psi_{\mathrm{up}}(t)\rangle=a_1(t)|1\rangle+a_2(t)|2\rangle, \tag{4.1}$$

it can be shown [22] that the dynamics of the two upper levels is governed by the Schrödinger equation

$$i\frac{d}{dt}\begin{pmatrix}a_1(t)\\ a_2(t)\end{pmatrix}=\overline{H}_{\mathrm{mod}}\begin{pmatrix}a_1(t)\\ a_2(t)\end{pmatrix}, \tag{4.2}$$

with

$$\overline{H}_{\mathrm{mod}}\equiv\begin{pmatrix}E_1-i\Gamma_1/2 & w\\ w & E_2-i\Gamma_2/2\end{pmatrix}, \tag{4.3}$$

where E_1 and E_2 are the energies, w is the coupling strength, and Γ_1 and Γ_2 are the decay rates of the upper levels. The population of the third level is simply $P_3(t)=1-P_1(t)-P_2(t)$, where $P_1(t)=|a_1(t)|^2$ and $P_2(t)=|a_2(t)|^2$. Equation (4.2) can be solved analytically by diagonalizing $\overline{H}_{\mathrm{mod}}$. If $|\eta\rangle$, $|\xi\rangle$ are the eigenstates of $\overline{H}_{\mathrm{mod}}$ with eigenenergies ε_η and ε_ξ, the solution is

$$|\psi_{\mathrm{up}}(t)\rangle=a_\xi(0)e^{-i\epsilon_\xi t}|\xi\rangle+a_\eta(0)e^{-i\epsilon_\eta t}|\eta\rangle, \tag{4.4}$$

$$a_\xi(0)=a_1(0)\langle\xi|1\rangle+a_2(0)\langle\xi|2\rangle, \tag{4.5}$$

$$a_\eta(0)=a_1(0)\langle\eta|1\rangle+a_2(0)\langle\eta|2\rangle. \tag{4.6}$$

In Figs. 2 and 3 we analyze the time evolution of this three-level system as a function of the propagation distance $d=v_p t$. The energies and radiative decay rates have been

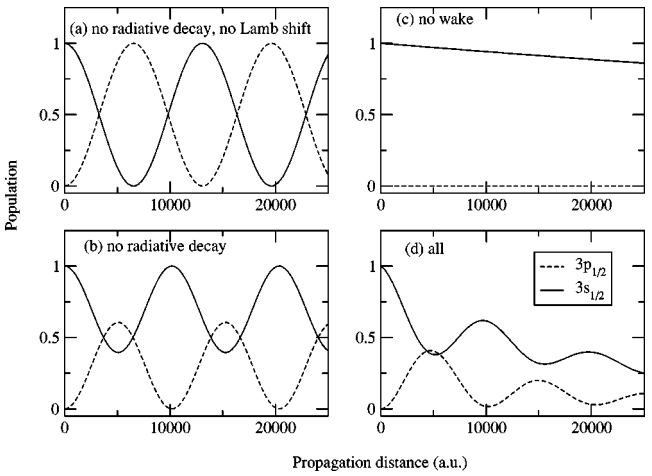

FIG. 3. Population dynamics as in Fig. 2 but in $n=3$ shell obtained within a three-state model involving the $3s_{1/2}$ and $3p_{1/2}$ states as upper levels and the $1s_{1/2}$ state as the lower level. Atomic structure parameters: Lamb shift, $|\Delta E|=1.9\times10^{-2}$, the radiative decay rates $\Gamma_{3s_{1/2}}=2.9454\times10^{-4}$, $\Gamma_{3p_{1/2}}=7.6762\times10^{-3}$ [16], Stark coupling due to the wake field, 1.176×10^{-2} [16], all in a.u. Some of these parameters are set to zero in (a), (b), and (c). Initially, at $d=0$, $P_{3s_{1/2}}(0)=1$, $P_{3p_{1/2}}(0)=0$, and $P_{1s_{1/2}}(0)=0$.

chosen such that in Fig. 2, the two upper levels 1 and 2, respectively, represent the $2s_{1/2}$ and $2p_{1/2}$ states whereas in Fig. 3 the two upper levels represent the $3s_{1/2}$ and $3p_{1/2}$ states of Kr^{35+}, all of them for a fixed value $m_j=1/2$. The d states of the $n=3$ shell are neglected in this simplified-model system. The level splitting $\Delta E=E_1-E_2$ between the levels is given by the Lamb shift. The value of the coupling-matrix element w between states 1 and 2 is set each to the coupling strength between the states due to the wake field for Kr^{35+} at a speed of $v_p=47$ a.u. The initial condition is chosen such that state $|1\rangle$ (the $ns_{1/2}$ state) is occupied with unit probability. In panel (a), the Lamb shift is set to zero, i.e., $\Delta E=0$ and the radiative decay is turned off. In this case, both states are completely mixed by the wake field. In panel (b), the Lamb shift is turned on by which the mixing due to the wake field is considerably reduced. The effective degree of mixing depends of the ratio of the coupling w to the level splitting $|\Delta E|$. For $n=2$, $|\Delta E|=6.3\times10^{-2}$ a.u.$\gg w=5.43\times10^{-3}$ a.u. and, therefore, Stark mixing is almost completely suppressed. In turn, for $n=3$, $|\Delta E|=1.9\times10^{-2}$ a.u.$\sim w=1.176\times10^{-2}$ a.u. [16] and a considerable amount of mixing can take place. In panel (c) of Figs. 2 and 3, we turn on the radiative decay but turn off the wake field. Since the system is initially in the $s_{1/2}$ states, the population of the $p_{1/2}$ states remains equal to zero for all times. Since the $2s_{1/2}$ state is metastable, its population is approximately constant. In panel (d), we turn on the wake and, therefore, $p_{1/2}$ states acquire a finite population. Note that this population is much larger in $n=3$ than in $n=2$ because of the larger ratio of Stark coupling to level splitting. Clearly, the population dynamics within a given n shell strongly depends on the relative size of the wake field, the Lamb shift, and the radiative decay rate. Thus, any realistic simulation must consider their combined effects in the full transport simulation. Since the

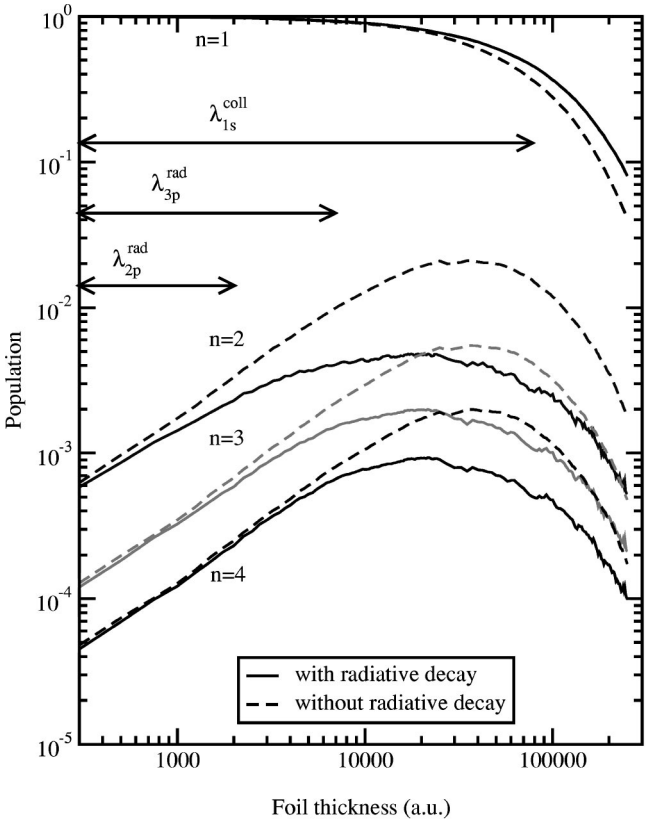

FIG. 4. Analysis of the effect of radiative decay on the populations of the $n=1$, 2, 3, and 4 shells at foil exit, $P_n(d)$. Solid lines: calculations with radiative decay. Dashed lines: calculations without radiative decay. The horizontal arrows indicate the mean free paths for the collisional excitation from the $1s$ state and for radiative decay.

populations for $n=3$ exhibit the most pronounced effects, we will mainly focus on the dynamics of this shell.

Figure 4 displays results for the populations of different n shells at the foil exit,

$$P_n(d)=\sum_{l,j,m_j} P_{n,l,j,m_j}(d), \tag{4.7}$$

of realistic transport simulations including multiple collisions and with the radiative decay during transport either switched off or on. As a function of foil thickness, the populations of excited states first increase monotonically and subsequently decrease monotonically for foil thicknesses larger than $\lambda_{1s}^{\rm coll}$ since the ''source'' state $1s$ of Kr begins to be depleted and ionization starts playing an important role. For simulations without radiative decay, the populations of excited states approximately maximize at a thickness $d\sim\lambda_{1s}^{\rm coll}$ (depicted by a horizontal arrow). In the presence of radiative decay, however, the positions of the maxima move towards smaller d. The presence of radiative decay becomes visible at foil thicknesses of the order of the fastest radiative mean free path within a given manifold (e.g., for $n=2$, when $d\sim\lambda_{2p}^{\rm rad}$).

The maximum foil thickness utilized in our experiment is 2.5×10^4 a.u.. In this range of thicknesses, the populations do

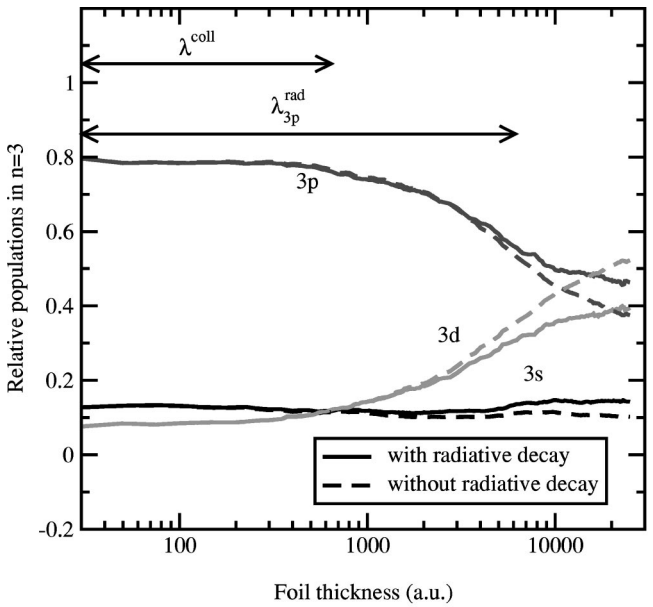

FIG. 5. Analysis of the effect of radiative decay on the subshell relative populations within the $n=3$ level at foil exit. Solid lines: calculations with radiative decay. Dashed lines: calculations without radiative decay. The horizontal arrows indicate the collisional and radiative-decay mean free paths.

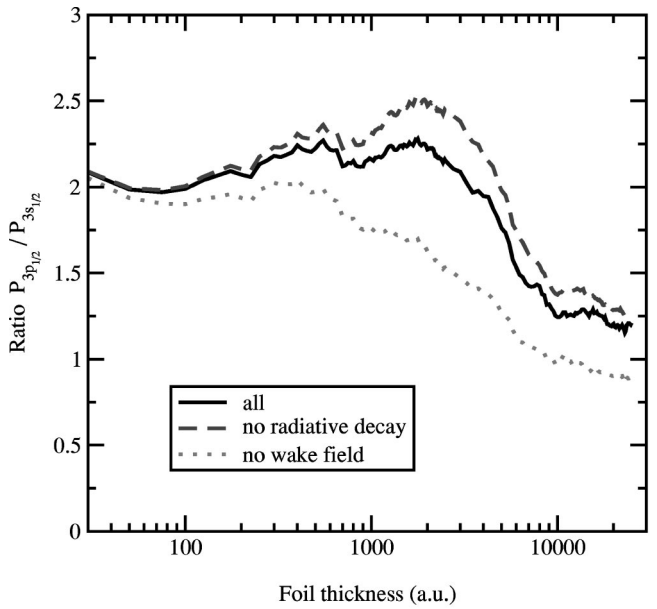

FIG. 6. Ratio between the populations of the $3p_{1/2}$ and $3s_{1/2}$ states at foil exit. Solid line: full simulation. Dashed line: calculation without radiative decay but with wake field. Dotted line: calculation without the wake field but with radiative decay.

not reach the maxima of the n-shell populations shown in Fig. 4 and, hence, excited states are mostly populated by direct transitions from the ground state rather than from multiple excitations involving several n levels. In turn, there exists a larger degree of intrashell collisional mixing compared to other systems studied in the past. All the calculations in the following were performed using an expansion of the wave function of the projectile electron in a basis set involving hydrogenic bound states of the ion up to $n=6$, which corresponds to a total number of 182 states. Typical simulations involved $N_{\mathrm{traj}}=10^4$ quantum trajectories. The ionization probability in our experiment is relatively small and, therefore, using this truncated basis is a good approximation. Note that the transitions form factors allow direct transitions from the states in the basis to states outside the basis set (i.e., the complement of the basis set, including transitions to the continuum). However, transitions from the complement back into the truncated basis set are neglected. The norm of the wave function provides a good indication of the total loss of probability due to the transition to the complement. In the present application, the norm remains close to unity. For $V_{\mathrm{sc}}(\vec{r})$, we use the dipole approximation with an n-dependent electric field from Ref. [16]. We have tested the accuracy of the resulting Stark couplings and energy levels against calculations we performed using a more elaborate approach in which the wake field was obtained in linear response theory from the dielectric function of Ashley and coworkers [28].

Figure 5 displays the *relative* populations of n, ℓ subshells in $n=3$ as a function of foil thickness, i.e., the populations at each foil thickness are normalized to the total population in the $n=3$ shell. For thin foils, the populations are nearly constant reflecting the ratios of direct transition probabilities from the ground state of Kr to different final states under single-collision conditions. Note that the population of the ''source'' state is still almost constant. The curves start to separate from the single-collision limit at a foil thickness $d\sim 10^3$ a.u., which is of the order of the collisional mean free path for transport of free electrons, λ^{coll} (depicted by a horizontal arrow). In turn, results with and without radiative decay during transport start to separate from each other for foil thicknesses of the order $d\sim\lambda_{3p}^{\mathrm{rad}}$. Without radiative decay, the relative populations approach the statistical limit for intrashell mixing, i.e., $P_{3s}:P_{3p}:P_{3d}=2:6:10$. Simulations with radiative decay during transport indicate that radiative decay effectively slows down intrashell mixing. The reason for this, at first glance, puzzling finding, is as follows: a single collision from the $1s$ ''source state'' mostly populates the $3p$ orbital. For increasing foil thicknesses, the populations of the $3s$ and $3d$ orbitals are, in addition to their direct excitation from the $1s$ state, enhanced by a second source, the intrashell redistribution from the $3p$ orbital. However, when the foil thickness exceeds the $3p$ radiative decay mean free path, the absolute $3p$ population decreases compared to the case without radiative decay (see Fig. 4) and, hence, the $3d$ and $3s$ states begin to lose one source of their enhanced population. Note that even though the $3s$ and $3p$ *relative* populations obtained with radiative decay during transport are larger than those without radiative decay in the thick-foil region, this certainly does not mean that radiative decay increases the *absolute* population of these states. This observation is key to understanding of the enhancement of the population ratios $3p_{1/2}$ to $3s_{1/2}$ as a function of the foil thickness (Fig. 6) in the presence of radiative decay. The effect is further enhanced by the wake field. While with the wake field turned on, a pronounced maximum develops near $d\approx 2000$ a.u., switching off the wake

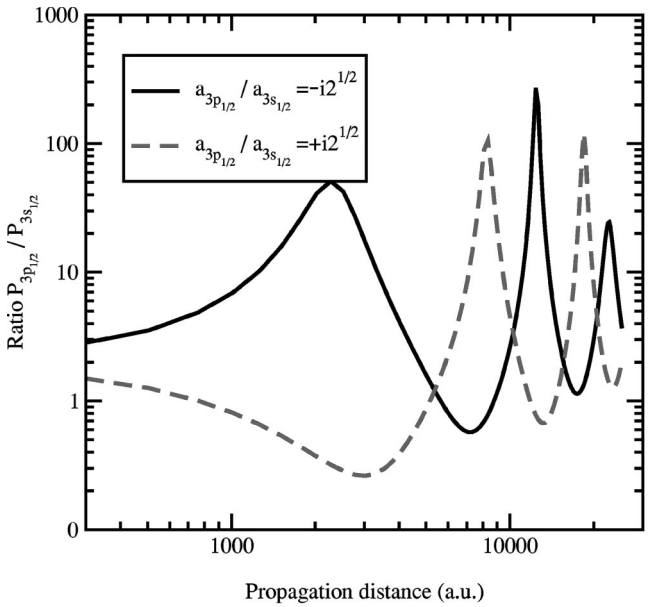

FIG. 7. Ratio between the populations of the $3p_{1/2}$ to $3s_{1/2}$ states for different initial coherences. The calculations were performed within a three-state model involving the $3s_{1/2}$ and $3p_{1/2}$ states as upper levels and the $1s_{1/2}$ state as the lower level and neglecting multiple collisions. Initially, the electron is in a coherent superposition of the two upper levels such that the ratio of the amplitudes is $a_{3p_{1/2}}/a_{3s_{1/2}} = \pm i\sqrt{2}$.

field leads to a reduction of this population ratio. Both wake-field effects and radiative decay are crucial in order to understand the experimental population ratio discussed below.

There is a third ingredient that needs to be included in order to reproduce the experimental photon-intensity ratios: the collisionally induced coherences between the *s* and the *p* states, i.e., the off-diagonal elements of the density matrix under single-collision conditions. In order to illustrate the importance of the initial coherences, we consider in Fig. 7 the simplified three-level model discussed above [Eq. (4.2)] where the two upper levels represent the $3s_{1/2}$ and $3p_{1/2}$ states for an extreme case of a fully coherent initial state with either $a_{3p_{1/2}}/a_{3s_{1/2}} = -i\sqrt{2}$ or $a_{3p_{1/2}}/a_{3s_{1/2}} = +i\sqrt{2}$. The first choice is not arbitrary but it approximately corresponds to the actual value obtained in our full QTT simulations under single-collision conditions. A relative phase of $\pm\pi/2$ between the *s* and the *p* amplitude is also consistent with the Born approximation, which gives rise to coherences of odd PT symmetry [29]. Choosing the negative sign of the phase, the ratio initially increases, reaches a maximum, and subsequently decreases, much like the result of the full simulations in Fig. 6 (the subsequent oscillations observed in the simplified model for thick foils are not observed for the real collision system because of damping due to multiple collisions). On the contrary, the ratio obtained with an initial phase rotated by π initially decreases, reaches a minimum, and subsequently increases (i.e., the oscillations are phase shifted by π). Clearly, since the two levels are coupled by the wake field, the initial coherence between the two levels plays a crucial role in the time evolution of the photon intensity ratio for thin foils [30].

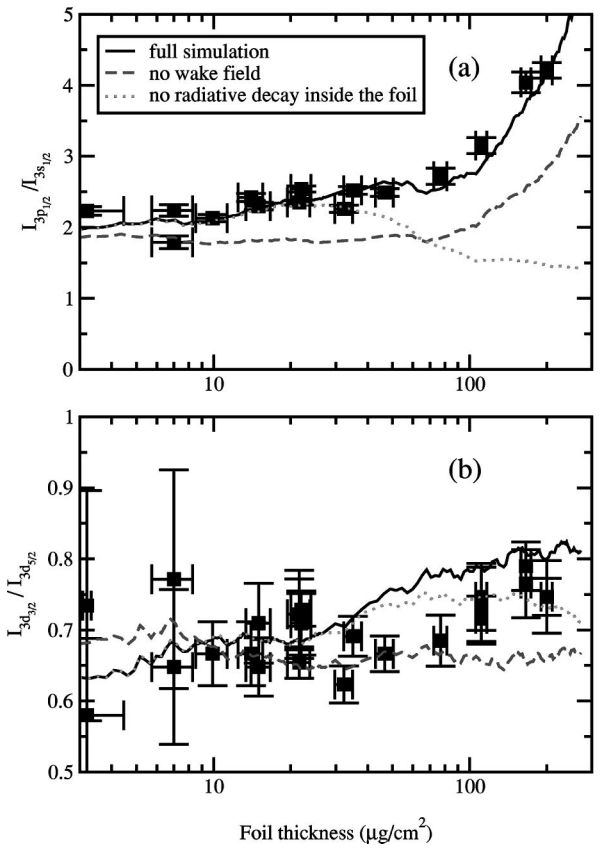

FIG. 8. Total intensity ratios as a function of foil thickness: (a) $I_{3p_{1/2}}/I_{3s_{1/2}}$ [Eq. (3.1)], (b) $I_{3d_{3/2}}/I_{3d_{5/2}}$ [Eq. (3.2)]. Symbols with error bars: experiment. Solid lines: full simulation. Dashed lines: calculation without the wake field. Dotted lines: calculation without radiative decay inside the foil.

The combined effects of initial coherence, the wake field, and radiative decay during transport are directly observable in the experiment. In Fig. 8 we compare the experimental and theoretical results of the full QTT for the ratio of intensities $I_{3p_{1/2}}/I_{3s_{1/2}}$ and $I_{3d_{3/2}}/I_{3d_{5/2}}$. The ratio of the intensities of *d* states is relatively insensitive and its value is very close to the single-collision value for all foil thicknesses. In turn, the ratio $I_{3p_{1/2}}/I_{3s_{1/2}}$ is very sensitive and changes by more than a factor of 2 within the range of foil thicknesses can be observed. In the thin-foil region, the radiative-decay mean free path is longer than the foil thickness and the intensity of photons emitted inside the foil is negligible. In fact, simulations with and without radiative decay during transport yield approximately the same result. However, the results for thick foils are quite different. The calculated ratio $I_{3p_{1/2}}/I_{3s_{1/2}}$ obtained from the full QTT simulation increases for increasing foil thickness whereas calculations neglecting radiative decay during transport give a decreasing ratio for thick foils. Also, only calculations with the proper coherence phase and including the wake field induced by the ion can account for the behavior of the experimental data.

V. CONCLUSIONS

In this paper we have presented a comparison between a quantum-mechanical transport theory (QTT) for the transport

of internal states of ions through thin foils with experimental data. In order to explain the experimental findings, the incorporation of radiative-decay, fine-structure, and Lamb-shift splittings as well as the wake-field coupling into the present stochastic Hamiltonian for the open quantum system was necessary. Radiative decay and collisional excitation was treated on equal footing within a quantum-trajectory Monte Carlo technique. Our simulation revealed that radiative decay inside the foil effectively slows down the mixing between the states. Our simulations showed that the wake field is not strong enough to mix the states with different j quantum numbers in any of the low-lying shells observed in the experiment. In turn, the wake-field coupling can be comparable with the Lamb splitting. Stark mixing modified by the Lamb shift was clearly observed for the $3s_{1/2}$ and $3p_{1/2}$ states. We also found that effects due to coherences generated by the primary direct-excitation process from the ground state of Kr can be identified in the experimental data due to the interplay of wake-field mixing and initial-state coherences.

ACKNOWLEDGMENTS

This work was supported by the NSF and FWF (Austria). C.O.R. acknowledges support by the DCS, OBES. U.S. DOE managed by UT-Battelle, LLC under Contract No. DE-AC05-00OR22725. We thank the University of Paris 6 et 7 for allowing us to organize a working meeting with B.G., J.B., and C.O.R. We also wish to extend our thanks to L. Adoui, A. Cassimi, J-P. Grandin, H. Rothard, and C. Stéphan for their participation in the data acquisition. We acknowledge J-M. Ramillon from the CIRIL for his technical support and the exploitation staff of the GANIL for providing us assistance and high-quality beams.

[1] P. Echenique, W. Brandt, and R. H. Ritchie, Phys. Rev. B **33**, 43 (1986).
[2] P. M. Echenique, F. Flores, and R. H. Ritchie, Solid State Phys. **43**, 229 (1990).
[3] J. Kemmler, J. Burgdörfer, and C. O. Reinhold, Phys. Rev. A **44**, 2993 (1991).
[4] C. O. Reinhold, D. G. Arbó, J. Burgdörfer, B. Gervals, E. Lamour, D. Vernhet, and J-P. Rozet, J. Phys. B **33**, L111 (2000).
[5] J. Burgdörfer and J. Gibbons, Phys. Rev. A **42**, 1206 (1990).
[6] Y. Yamazaki *et al.*, Phys. Rev. Lett. **61**, 2913 (1988).
[7] P. Nicolai, M. Chabot, J. P. Rozet, M. F. Politis, A. Chetioui, C. Stéphan, A. Touati, D. Vernhet, and K. Wohrer, J. Phys. B **23**, 3609 (1990).
[8] J. Burgdörfer and C. Bottcher, Phys. Rev. Lett. **61**, 2917 (1988).
[9] J. P. Rozet, C. Stéphan, and D. Vernhet, Nucl. Instrum. Methods Phys. Res. B **107**, 67 (1996).
[10] H. D. Betz, D. Röschenthaler, and J. Rothermel, Phys. Rev. Lett. **50**, 34 (1983); J. Rothermel, H. D. Betz, and F. Bell, Nucl. Instrum. Methods Phys. Res. **194**, 341 (1982).
[11] C. Can, R. J. Maurer, B. Bandong, and R. L. Watson, Phys. Rev. A **35**, 3244 (1987).
[12] D. Vernhet, J. P. Rozet, E. Lamour, B. Gervais, C. Fourment, and L. J. Dubé, Phys. Scr., T **T80A**, 83 (1999).
[13] D. G. Arbó, C. O. Reinhold, P. Kürpick, S. Yoshida, and J. Burgdörfer, Phys. Rev. A **60**, 1091 (1999).
[14] D. G. Arbó, C. O. Reinhold, S. Yoshida, and J. Burgdörfer, Nucl. Instrum. Methods Phys. Res. B **164–165**, 495 (2000).
[15] D. Vernhet, C. Fourment, E. Lamour, J-P. Rozet, B. Gervais, L. J. Dubé, F. Martin, T. Minami, C. O. Reinhold, M. Seliger, and J. Burgdörfer, Phys. Scr. **T92**, 233 (2001).
[16] J-P. Rozet, D. Vernhet, I. Bailly-Despiney, C. Fourment, and L. J. Dubé, J. Phys. B **32**, 4677 (1999).
[17] T. Minami, C. O. Reinhold, and J. Burgdörfer (unpublished).
[18] B. H. Bransden and C. J. Joachain, *Physics of Atoms and Molecules* (Longman Scientific and Technical, Harlow, 1983); W. R. Johnson and G. Soff, At. Data Nucl. Data Tables **33**, 405 (1985).
[19] J. Dalibard, Y. Castin, and K. Mølmer, Phys. Rev. Lett. **68**, 580 (1992); K. Mølmer, Y. Castin, and J. Dalibard, J. Opt. Soc. Am. B **10**, 524 (1993).
[20] R. Dum, P. Zoller, and H. Ritsch, Phys. Rev. A **45**, 4879 (1992); C. W. Gardiner and P. Zoller, *Quantum Noise* (Springer, 1999).
[21] U. Fano, Rev. Mod. Phys. **29**, 74 (1957).
[22] C. Cohen-Tannoudji, J. Dupont-Roc, and G. Grynberg, *Atom-Photon Interactions* (Wiley-Interscience, New York, 1992).
[23] H. Bethe and F. Salpeter, *Quantum Mechanics of One- and Two-Electron Atoms* (Plenum, New York, 1977).
[24] V. G. Pal'chikov, Phys. Scr. **57**, 581 (1998).
[25] B. Gervais, C. O. Reinhold, and J. Burgdörfer, Phys. Rev. A **53**, 3189 (1996).
[26] P. Kürpick, C. O. Reinhold, J. Burgdörfer, and B. Gervais, Phys. Rev. A **58**, 2183 (1998).
[27] D. Vernhet, J-P. Rozet, I. Bailly-Despiney, C. Stéphan, A. Cassimi, J-P. Grandin, and L. J. Dubé, J. Phys. B **31**, 117 (1998).
[28] J. Ashley, C. Tung, and R. Ritchie, Surf. Sci. **81**, 409 (1979); C. Martin, E. Arakawa, T. Callcott, and J. Ashley, J. Electron Spectrosc. Relat. Phenom. **35**, 307 (1985); J. Ashley, J. Cowan, R. Ritchie, V. E. Anderson, and J. Hoelzel, Phys. Thin Films **60**, 361 (1979); J. Ashley, J. Electron Spectrosc. Relat. Phenom. **28**, 177 (1982).
[29] J. Burgdörfer, in *Fundamental Processes of Atomic Dynamics*, edited by J. Briggs, H. Kleinpoppen, and H. O. Lutz (Plenum, New York, 1988), pp 159–176.
[30] T. Minami, C. O. Reinhold, M. Seliger, J. Burgdörfer, C. Fourment, B. Gervais, E. Lamour, J-P. Rozet, and D. Vernhet, Nucl. Instrum. Methods Phys. Res. B (to be published).